Cross-flow, solid-state electrochemical reactors: a steady state analysis

Costas G. Vayenas, Pablo G. Debenedetti, Iannis Yentekakis, and L. Louis Hegedus

More About This Article

The permalink http://dx.doi.org/10.1021/i100019a007 provides access to:

- Links to articles and content related to this article
- Copyright permission to reproduce figures and/or text from this article

Cross-Flow, Solid-State Electrochemical Reactors: A Steady-State Analysis

Costas G. Vayenas and Pablo G. Debenedetti

Department of Chemical Engineering, Massachusetts Institute of Technology, Cambridge, Massachusetts 02139

Iannis Yentekakis

Department of Chemical Engineering, University of Patras, Patras, Greece

L. Louis Hegedus*

W. R. Grace & Company, Research Division, Columbia, Maryland 21044

The cross-flow monolith is a novel solid-state electrocatalytic reactor configuration. The solid-state reactor, in principle, can be used to generate electricity, co-generate electricity and useful chemicals, enhance the rate of certain catalytic reactions, or to electrolyze O-containing compounds. The distinguishing feature of the cross-flow geometry is its inherently high O^{2-} transfer area per unit volume, which gives rise to higher calculated power densities than conventional designs. A two-dimensional mixing cell model was constructed to stimulate the distribution of species, temperature, and current density. Results are reported for the species conversion, temperature distribution, thermodynamic energy conversion efficiency, and volumetric power density of a model reaction (CO oxidation over Pt in an yttria-doped zirconia structure).

Introduction

One of the emerging uses of solid-state electrocatalytic systems is in fuel cells, to convert a significant portion of the Gibbs free energy change of exothermic reactions into electricity rather than heat. The thermodynamic efficiency of such power generating schemes compares favorably with thermal power generation which is limited by Carnot-type constraints.

Solid-electrolyte fuel cells, operating on H_2 or CO as the fuel, have been constructed and tested for years (Archer et al., 1965; Etsell and Flengas, 1971). Similar devices have been used for steam electrolysis (Weissbart et al., 1969), for NO decomposition (Gur and Huggins, 1979), and for methane synthesis from CO and H_2 (Gur and Huggins, 1981).

Zirconia cells with Pt catalyst-electrodes can also be used to convert ammonia to nitric oxide with simultaneous electrical energy generation (Vayenas and Farr, 1980; Sigal and Vayenas, 1981). A number of other industrially important oxidations have been recently proposed for solid-state electrocatalytic reactors, such as the conversion of sulfur to SO_2 or SO_3 (Yang et al., 1982), or ethylene epoxidation (Stoukides and Vayenas, 1982).

The practical usefulness of these electrochemical converters is partly a function of their volume power densities. This parameter is composed of the oxygen ion transfer area per unit reactor volume (cm^2/cm^3) multiplied by the power density per unit oxygen ion transfer area (W/cm^2). Previous fuel cells (Archer et al., 1965; Federmann et al., 1981) exhibited volume power densities in the range 300–400 W/L; the fuel cell configuration we describe here has the potential of further increasing this number, primarily by increasing the oxygen ion transfer area per unit reactor volume by about a factor of 4 to 5.

Cross-flow monoliths have been explored by Degnan and Wei (1979, 1980) as cocurrent and countercurrent reactor-heat exchangers. Four cross-flow monoliths in series were employed; the individual blocks were analyzed by a one-dimensional approximation. They found good agreement between theory and experiment.

Roy and Gidaspow (1972, 1974) developed two-dimensional continuum models to describe cross-flow monolithic heat exchangers and catalytic reactors.

Despite the geometric similarities, the problem analyzed here is fundamentally different from that of cross-flow heat exchangers or catalytic reactors in that the solid is not only used as a heat-exchange medium or as a catalyst support but also as the electrolyte across which oxygen ion transport occurs. This introduces an integral electron conservation balance which results in an integro-differential problem.

The modeling of single-cell, solid-state electrocatalytic reactors was recently discussed by Debenedetti and Vayenas (1983); this paper's objective is to develop an analysis for cross-flow monolithic designs.

Reactor Configuration

A schematic diagram of a cross-flow monolith fuel cell reactor is given in Figure 1. The reactor consists of two sets of channels in the x and y direction, respectively.

Channels in the x direction serve for the oxidant flow. Their surface is coated with a catalyst such as Pt or Ag which facilitates the reduction of O_2 to O^{2-}. Since yttria-doped zirconia is a pure O^{2-} conductor, the oxygen ions migrate through the solid electrolyte wall to channels y which serve for the fuel flow.

Channels y are perpendicular to channels x and the two alternate along the z axis of the monolith. The walls of channels y are coated with a suitable metal or conductive
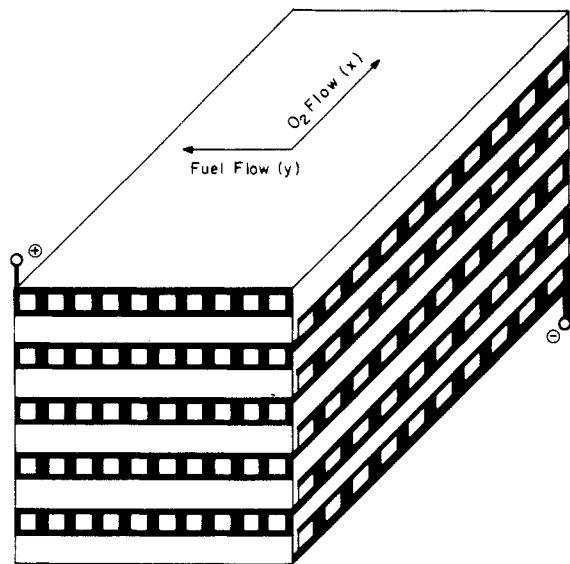
Figure 1. Schematic diagram of a cross-flow monolith fuel cell consisting of $Z = 5$ unit batteries connected in series. Each unit battery consists of 100 unit cells electrically connected in parallel. Dark areas on monolith's faces are covered with conductive metal film.

metal oxide catalyst which catalyzes the fuel's anodic oxidation.

The fuel can be either inorganic such as hydrogen, carbon monoxide, ammonia, sulfur vapor, sulfur dioxide, or organic such as methane or methanol. Other fuels can of course also be used; depending on the nature of the fuel and that of the desired partial or complete oxidation product, one must use different catalyst–electrode materials in channels y. Thus one can use Pt for ammonia conversion to NO (Vayenas and Farr, 1980) or for H_2 and CO combustion (Etsell and Flengas, 1971), Ag for ethylene epoxidation (Stoukides and Vayenas, 1982), or complex base metal oxide systems for H_2 and CO oxidation (Federmann et al., 1981).

One restriction regarding the nature of the catalyst coated on the walls of channels x and y is that it must be electrically conductive but also reasonably porous so that it allows the access of fuel or O_2 molecules to the solid electrolyte–catalyst–gas three-phase boundary.

Porous and highly conductive Pt, Ag, and In_2O_3 films can be deposited on zirconia (Etsell and Flengas, 1971; Stoukides and Vayenas, 1982; Gur and Huggins, 1979).

Although the present analysis is focused on the case of CO oxidation to CO_2, the application of the model to other oxidation reactions is quite straightforward.

Considering the oxidation reaction

$$nA + O_2 \rightarrow nB \tag{1}$$

the following reactions take place at the cathode, i.e., x channels and anode, i.e., y channels, respectively

$$O_2 + 4e^- \rightarrow 2O^{2-} \tag{2}$$

$$nA + 2O^{2-} \rightarrow nB + 4e^- \tag{3}$$
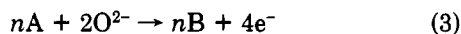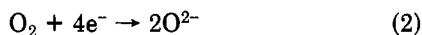
Thus the net effect is the conversion of A into product B and simultaneous electrical energy generation.

Under low current density conditions, i.e., at very large external loads, a large fraction of the Gibbs free energy change of the oxidation reaction 1 is converted into electrical energy. At higher current densities, the cell voltage E drops from its equilibrium value E_{rev}.

In the absence of activation and concentration polarization, the power output $P = EI$ of the cell is maximized when the external resistance R_{ex} equals the internal resistance of the cell.
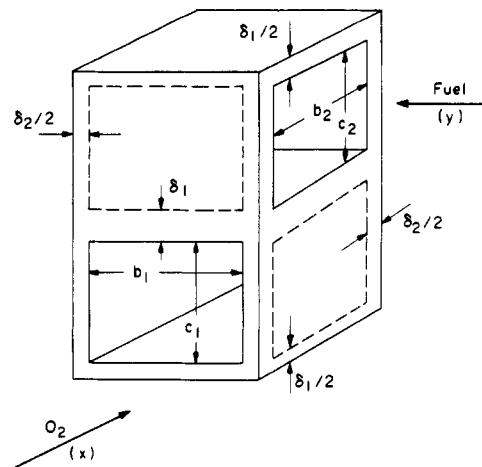

Figure 2. Schematic diagram of a unit cell.

The thermodynamic cell efficiency η is usually defined as the dimensionless cell voltage

$$\eta = E/E_{th} = W/(-\Delta H°) \tag{4}$$

where the thermoneutral voltage E_{th} is given by

$$E_{th} = n(-\Delta H°)/4F \tag{5}$$

and W is the electrical work produced per mole of fuel. Since, in general

$$E = E_{rev} - \phi_{ohm} - \phi_{act.} - \phi_{conc} \tag{6}$$

and

$$E_{rev} = n(-\Delta G)/4F = n(-\Delta H + T\Delta S)/4F \tag{7}$$

it follows from (4) through (7) that for low current densities, i.e., for low values of ϕ_{ohm}, ϕ_{act}, and ϕ_{conc}, the cell efficiency η can exceed unity for reactions with positive ΔS, such as NH_3 oxidation to NO, but will be less than 1 (about 0.75) for CO oxidation, even at vanishing current densities, due to the negative ΔS associated with this reaction.

A differential reactor is implicit in the above statements, since species conversion can markedly affect operating voltage, and efficiency values as defined in (4) can easily exceed one even for negative ΔS systems in other reactor types.

Mathematical Model

The geometry of the reactor is depicted in Figure 1. We assume that the top and bottom surfaces are insulated, so that there is no net heat flux in the z direction and thus the problem becomes two-dimensional.

There is of course no net mass flow in the z direction, except for that of the O^{2-} ions inside the electrolyte which is accounted for in the electron balance equations.

For modeling purposes, the reactor is considered to be composed of unit cells. One such unit cell is shown in Figure 2.

There are K times L such unit cells in each unit battery and KLZ unit cells in the entire reactor. The unit cells are labeled 1, 2, ..., k, ..., K in the x direction (oxidant flow), 1, 2, ..., l, ..., L in the y direction (fuel flow), and they are stacked along the z direction but not indexed due to the two-dimensional nature of the problem.

The unit batteries, as shown in Figure 1, are connected in series. The model formulation includes both series and parallel unit battery configurations. However, all numerical runs were carried out for the series configuration.

Within each unit cell, we assumed uniform solid temperature and uniform gas-phase composition and temperature for both streams. However, the (uniform) fuel and oxidant stream temperatures are, of course, different

from each other and from the solid temperature.

The model consists of a description of events occurring in a unit cell and of a description of how this unit cell communicates with surrounding unit cells. Thus, the model's structure will appear in the form of a large number of coupled algebraic equations.

Fuel Channel Mass Balance. Since the current produced by an electrocatalytic reaction is related to the conversion of reactive species, we can express the local mass balances in terms of local current densities, using Faraday's law.

Thus, for the fuel A in cell (k,l) we obtain

$$\lambda i_{k,l} = N_A \left(\frac{4F}{n} \right) \frac{c_2}{b_1} (X_{A,k,l} - X_{A,k,l-1}) \tag{8}$$

Defining a dimensionless local current density as

$$\xi_{k,l} = \frac{i_{k,l}}{N_A \left(\dfrac{4F}{n} \right) \dfrac{c_2}{b_1}} \tag{9}$$

and substituting it into (8), we obtain a dimensionless fuel conservation equation in the form of

$$\lambda \xi_{k,l} = (X_{A,k,l} - X_{A,k,l-1}) \tag{10}$$

where $\lambda = 1$ for series connection of unit batteries with insulating plates between adjacent unit batteries (as shown in Figure 1) and $\lambda = 2$ for parallel connection of unit batteries.

The choice of parallel or series connections, or their combinations, allows one to manipulate the internal resistance of the unit in order to maximize its power output for a desired value of external load.

In principle, parallel connection doubles the effective oxygen ion transfer surface area when compared with series connection, since the entire geometric electrolyte surface is utilized for oxygen ion transfer. This is a consequence of the geometry of the cross-flow monolith configuration.

Oxidant Channel Mass Balance. Using the Faraday relationship for the fuel, the consumption of oxygen in the oxygen channel of unit cell (k,l) becomes

$$\lambda i_{k,l} = N_{O_2}(4F) \frac{c_1}{b_2} (X_{O_2,k,l} - X_{O_2,k-1,l}) \tag{11}$$

Substituting the dimensionless current density $\xi_{k,l}$ from (9), we obtain

$$\lambda \xi_{k,l} = N_1 (X_{O_2,k,l} - X_{O_2,k-1,l}) \tag{12}$$

where

$$N_1 = \frac{N_{O_2}}{N_A} \times n \times \frac{c_1 b_1}{c_2 b_2} \tag{13}$$

Fuel Stream Energy Balance. The following components contribute to the heat balance of the gas phase of the fuel channel in unit cell (k,l)

$b_2 c_2 N_A (1 - X_{A,k,l-1}) C_{P,A} T_{F,k,l-1} +$
$\quad b_2 c_2 N_A X_{A,k,l-1} C_{P,B} T_{F,k,l-1} + b_2 c_2 N_D C_{P,D} T_{F,k,l-1}$
(convective enthalpy input from cell $(k,l-1)$) +
$[\lambda i_{k,l}/(4F/n)] b_1 b_2 C_{P,B} T_{S,k,l}$ (enthalpy gain through product transfer from solid) =
$\quad b_2 c_2 N_A (1 - X_{A,k,l}) C_{P,A} T_{F,k,l} +$
$b_2 c_2 N_A X_{A,k,l} C_{P,B} T_{F,k,l} + b_2 c_2 N_D C_{P,D} T_{F,k,l}$ (convective enthalpy loss to cell $(k, l + 1)$) +
$[\lambda i_{k,l}/(4F/n)] b_1 b_2 C_{P,A} T_{F,k,l}$ (enthalpy loss through reactant transfer to solid) + $2 h_F (b_1 + \delta_2)(b_2 + c_2)$
$(T_{F,k,l} - T_{S,k,l})$ (heat loss to solid through heat transfer)
$$\tag{14}$$

We define dimensionless temperatures as

$$\theta_F = T_F / T_{F,in} \tag{15}$$

$$\theta_S = T_S / T_{F,in} \tag{16}$$

with which, after algebraic rearrangement, one obtains

$$\theta_{F,k,l} - \theta_{F,k,l-1} = \frac{(\theta_{S,k,l} - \theta_{F,k,l})[N_2 + N_{11}(X_{A,k,l} - X_{A,k,l-1})]}{1 + N_3 + (N_{11} - 1)X_{A,k,l-1}} \tag{17}$$

where

$$N_2 = \frac{2 h_F (b_1 + \delta_2)(b_2 + c_2)}{b_2 c_2 N_A C_{P,A}} \tag{18}$$

$$N_3 = N_D C_{P,D} / N_A C_{P,A} \tag{19}$$

$$N_{11} = C_{P,B} / C_{P,A} \tag{20}$$

Oxidant Stream Energy Balance. Similar terms were considered for the oxidant compartment of the gas phase of unit cell (k,l), so it is not necessary to list them in detail.

The resulting dimensionless oxidant stream energy balance is

$$\theta_{OX,k,l} - \theta_{OX,k-1,l} = \frac{N_4(\theta_{S,k,l} - \theta_{OX,k,l})}{1 + N_5 - X_{O_2,k-1,l}} \tag{21}$$

with

$$\theta_{OX} = T_{OX} / T_{F,in} \tag{22}$$

$$N_4 = \frac{2 h_{OX}(b_2 + \delta_2)(b_1 + c_1)}{b_1 c_1 N_{O_2} C_{p,O_2}} \tag{23}$$

$$N_5 = N_{N_2} C_{P,N_2} / N_{O_2} C_{P,O_2} \tag{24}$$

Solid Energy Balance. The solid-phase energy balance is composed of terms related to thermal communication with the walls of neighboring unit cells, with the two gas-phase compartments of unit cell (k,l), and of the electrical work produced. For clarity, we have elected to show these terms in detail.

$\dfrac{k_s A_{S,F}(T_{S,k,l+1} - T_{S,k,l})}{(b_1 + \delta_2)} + \dfrac{k_s A_{S,F}(T_{S,k,l-1} - T_{S,k,l})}{(b_1 + \delta_2)} +$
$\dfrac{k_s A_{S,OX}(T_{S,k+1,l} - T_{S,k,l})}{(b_2 + \delta_2)} +$
$\dfrac{k_s A_{S,OX}(T_{S,k-1,l} - T_{S,k,l})}{(b_2 + \delta_2)} -$
(conductive input from neighboring cells)
$2 h_{OX}(b_2 + \delta_2)(b_1 + c_1)(T_{S,k,l} - T_{OX,k,l}) - 2 h_F (b_1 + \delta_2)(b_2 + c_2)(T_{S,k,l} - T_{F,k,l})$

(heat transfer from solid to gas) $+ b_1 b_2 \lambda \dfrac{i_{k,l}}{4F} C_{P,O_2} \times$

$(T_{OX,k,l} - T_{F,in}) + b_1 b_2 \lambda \dfrac{i_{k,l}}{(4F/n)} [C_{P,A}(T_{F,k,l} - T_{F,in}) +$

$H_A^\circ] - b_1 b_2 \lambda \dfrac{i_{k,l}}{(4F/n)} [C_{P,B}(T_{S,k,l} - T_{F,in}) + H_B^\circ] =$

$\lambda i_{k,l} b_1 b_2 E$ (electrical work produced by unit cell) $\tag{25}$

where

$$A_{S,F} = 2 \delta_1 (b_2 + \delta_2) + c_2 \delta_2 \tag{26}$$

$$A_{S,OX} = 2 \delta_1 (b_1 + \delta_2) + c_1 \delta_2 \tag{27}$$

Introducing the above-defined dimensionless temperatures and recalling the definition of η from (4), after appropriate algebraic manipulation we obtain

$$(\theta_{S,k,l+1} + \theta_{S,k,l-1} - 2\theta_{S,k,l}) + N_6(\theta_{S,k+1,l} + \theta_{S,k-1,l} - 2\theta_{S,k,l}) - N_7(\theta_{S,k,l} - \theta_{OX,k,l}) - N_8(\theta_{S,k,l} - \theta_{F,k,l}) + \lambda N_9 \xi_{k,l}[N_{10}(\theta_{OX,k,l} - 1) + (\theta_{F,k,l} - 1) - N_{11}(\theta_{S,k,l} - 1) + N_{12}(1 - \eta)] = 0 \quad (28)$$

where

$$N_6 = \left(\frac{A_{S,OX}}{A_{S,F}}\right)\left(\frac{b_1 + \delta_2}{b_2 + \delta_2}\right) \quad (29)$$

$$N_7 = \frac{2h_{OX}(b_2 + \delta_2)(b_1 + c_1)(b_1 + \delta_2)}{k_S A_{S,F}} \quad (30)$$

$$N_8 = \frac{2h_F(b_1 + \delta_2)^2(b_2 + c_2)}{k_S A_{S,F}} \quad (31)$$

$$N_9 = \frac{b_2 c_2(b_1 + \delta_2)NC_{P,A}}{k_S A_{S,F}} \quad (32)$$

$$N_{10} = \frac{C_{P,O_2}}{nC_{P,A}} \quad (33)$$

$$N_{12} = \frac{(-\Delta H^\circ)}{C_{P,A}T_{F,in}} \quad (34)$$

Note that, despite the typically high operating temperatures of fuel cells, radiative heat transfer was neglected. Lee and Aris (1977) have discussed such effects in parallel-channel monoliths. The importance of radiative transport depends on the emissivity of the surface; for the low (about 0.1) emissivity of Pt-coated catalyst-electrodes, their analysis suggests that radiative effects can be neglected.

Electron Balance Equations. In order to solve the system of difference equations (10, 12, 17, 21, 28), it is necessary to express the local current density $\xi_{k,l}$ and the dimensionless cell voltage η in terms of local solid temperatures and gaseous compositions.

It can be shown that for typical thicknesses of solid electrolyte (say, 100 μm) and porous metal catalyst film (say, 10 μm), the major source of ohmic resistance (>99%) is the solid electrolyte. The consequence is that the actual dimensionless operating voltage η is constant along each channel and also constant for all channels electrically connected in parallel (as shown in Figure 1), i.e., constant within each unit battery. This observation significantly simplifies the development of the electron balance equations.

Considering an elementary unit cell (k,l), and neglecting activation and concentration overpotential, one obtains from (6)

$$E_{k,l} = E_{rev,k,l} - b_1 b_2 i_{k,l} R_{k,l} \quad (35)$$

where the last term represents the ohmic overpotential ϕ_{ohm}.

In most high-temperature, solid-electrolyte fuel cells, the major source of overpotential is ohmic (Archer et al., 1965; Etsell and Flengas, 1971; Farr and Vayenas, 1980).

Activation overpotential may become important with a number of electrocatalysts; however, as Debenedetti and Vayenas (1983) have discussed, the actual current–voltage behavior of the unit at moderate and high current densities can be well approximated by subtracting the activation overpotential from E_{rev}. For CO oxidation over Pt, this correction is not necessary if the feed contains 2–3 vol % H_2 or H_2O or if the catalyst contains small amounts of Cr_2O_3 (Archer et al., 1965).

Concentration overpotential arises due to external or internal mass transfer limitations. For typical cross-flow monoliths, Debenedetti (1981) has shown that concentration overpotential is negligible under conditions similar to those explored here. The analysis employed mass transfer coefficients for fully developed laminar flows in square ducts.

The unit cell resistance $R_{k,l}$ can be expressed in terms of the ionic resistivity of the solid electrolyte

$$R_{k,l} = \rho_{k,l}\frac{\lambda\delta_1}{b_1 b_2} \quad (36)$$

We also can express E_{rev} in terms of fuel and oxygen conversions employing the Nernst relationship. With these, from (36), and noting that $E_{k,l} = E$ for all k and l as discussed

$$E = E^\circ_{k,l} + \frac{nRT}{4F}\ln\left(P^\circ_{O_2}{}^{1/n}\right)\frac{(1 - X_{A,k,l})(1 - X_{O_2,k,l})^{1/n}}{X_{A,k,l}} - \rho_{k,l}i_{k,l}\lambda\delta_1 \quad (37)$$

Note again that although all right-hand terms in (37) are different for each unit cell, their sum (E) is invariant with unit cell conditions due to the high conductivity of the catalyst-electrode.

The electrolyte resistivity, $\rho_{k,l}$, exponentially depends on the local solid temperature

$$\rho_{k,l} = \rho_0 \exp\left[-\frac{E_{act.}}{RT_{F,in}}\left(1 - \frac{1}{\theta_{S,k,l}}\right)\right] \quad (38)$$

This can be substituted into (37).

To obtain a second equation between E and $i_{k,l}$, it is necessary to specify the nature of the electrical connections between the unit batteries.

Series Connection of Unit Batteries. In this case every second plate in the monolith is not covered with a catalyst-electrode.

The total voltage of the monolith can be computed from Kirchhoff's first law

$$ZE = \sum_{k=1}^{K}\sum_{l=1}^{L} b_1 b_2 i_{k,l}[(Z + 1)R_e + R_{ex}] \quad (39)$$

where Z is the number of unit batteries in the structure, R_e is the ohmic resistance of each connection between adjacent batteries, and R_{ex} is the external resistive load where the electrical power produced is dissipated.

Equations 37, 38, and 39 can be rearranged and expressed in dimensionless form as

$$\xi_{k,l} = \left[N_{13} + \left(N_{14} + N_{15} \times \ln\frac{P^\circ_{O_2}{}^{1/n}(1 - X_{A,k,l})(1 - X_{O_2,k,l})^{1/n}}{X_{A,k,l}}\right)\theta_{S,k,l} - N_{16}\sum_{k=1}^{K}\sum_{l=1}^{L}\xi_{k,l}\right]\exp\left[N_{17}\left(1 - \frac{1}{\theta_{S,k,l}}\right)\right] \quad (40)$$

$$\eta = N_{18}\sum_{k=1}^{K}\sum_{l=1}^{L}\xi_{k,l} \quad (41)$$

where

$$N_{13} = \frac{(-\Delta H^\circ)}{N_A(4F/n)^2\rho_o}\left(\frac{b_1}{c_2\delta_1\lambda}\right) \qquad (42)$$

$$N_{14} = \frac{(\Delta S^\circ)T_{F,in}}{N_A(4F/n)^2\rho_o}\left(\frac{b_1}{c_2\delta_1\lambda}\right) \qquad (43)$$

$$N_{15} = \frac{RT_{F,in}}{N_A(4F/n)^2\rho_o}\left(\frac{b_1}{c_2\delta_1\lambda}\right) \qquad (44)$$

$$N_{16} = \frac{b_1b_2[(Z+1)R_e + R_{ex}]}{Z\delta_1\rho_o\lambda} \qquad (45)$$

$$N_{17} = E_{act.}/RT_{F,in} \qquad (46)$$

$$N_{18} = \frac{b_2c_2(4F/n)^2N_A[(Z+1)R_e + R_{ex}]}{Z(-\Delta H^\circ)} \qquad (47)$$

It is interesting to note that $\xi_{k,l}$ in (40) is in fact equivalent to a dimensionless rate; the right side of the equation shows how the local rate depends on the concentrations (expressed as fractional conversions) of the reactants. The double summation indicates that the reaction rate is not only a function of local properties but also of the global performance of the reactor. This represents a feedback mechanism to each unit cell.

Parallel Connection of Unit Batteries. In this case there are only two external connections of resistance R_e. For a total of Z unit batteries it can be shown that the electron balance equations (40) and (41) remain valid, but the dimensionless numbers N_{16} and N_{18} will change

$$N_{16}(\text{parallel}) = \frac{b_1b_2(ZR_{ex} + 2R_e)}{\delta_1\rho_o\lambda} \qquad (48)$$

$$N_{18}(\text{parallel}) = \frac{b_2c_2(4F/n)^2N_A(ZR_{ex} + 2R_e)}{(-\Delta H^\circ)} \qquad (49)$$

Boundary Conditions. The boundary conditions of the problem arise through the appropriate specification of cells at the geometric boundaries of the cross-flow monolith body.

From the standpoint of mass balances, this required the specification of inlet concentrations. For the energy balances of the outer cell layers ($k = 1$ and K; and $l = 1$ and L), the specifications included perfect thermal insulation at the outer unit cell walls, to simulate adiabatic behavior.

Oxygen Ion Transfer Area per Unit Reactor Volume. As discussed above, the prime attraction of the cross-flow monolith configuration is its potentially high oxygen ion transfer area per unit reactor volume. From our unit cell (Figure 2), this volume-specific area computes as

$$S = \frac{\lambda b_1b_2}{(b_1+\delta_2)(b_2+\delta_1)(C_1+C_2+2\delta_1)} \qquad (50)$$

For the example employed in our calculations, $S = 3.76$ cm^2/cm^3. Within the limits of ceramics processability, this number, in principle, can be significantly increased.

Numerical Solution of the Equations

It should be noted that if a differential mass, energy, and electron balance approach were followed to describe the reactor's behavior, one would obtain a set of nonlinear, partial, integro-differential equations. However, since the reactor is simulated by a two-dimensional array of mixing cells, a large number of algebraic equations result in which there are no differentials and in which double integrals are replaced by double summations.
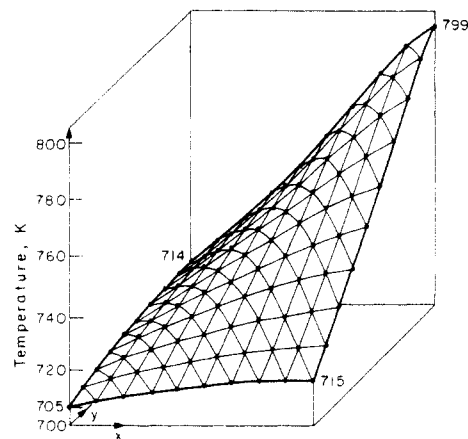

Figure 3. Two-dimensional solid temperature profile in a (3.3 × 3.3 cm) structure, corresponding to run 1 in Table I.

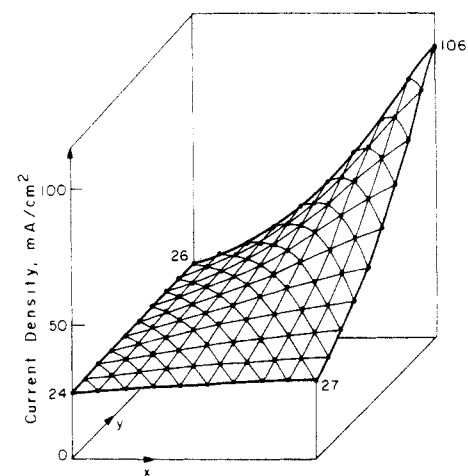**Figure 4.** Two-dimensional current density profile in a unit battery of a (3.3 × 3.3 cm) structure, corresponding to run 1 in Table I.

For a $K \times L$ array of unit cells, there is a total of 6 ($K \times L$) + 1 equations: 2 ($K \times L$) mass balances (eq 10 and 12), 3 ($K \times L$) energy balances (eq 17, 21, 28), $K \times L$ electron balances (eq 40), and one voltage equation (14). The corresponding 6 ($K \times L$) + 1 unknowns are 2 ($K \times L$) local fuel and oxidant conversions, 3 ($K \times L$) local fuel, oxidant, and solid temperatures, $K \times L$ local current densities, and the dimensionless operating voltage.

The solution is greatly simplified by realizing that of the 6 ($K \times L$) + 1 equations, only the ($K \times L$) electron balances are nonlinear.

Arbitrary initial values were given to the ($K \times L$) $\xi_{k,l}$ variables. Then the mass balance equations (10) and (12) were solved directly for all oxygen conversions $X_{O_2,k,l}$ and fuel conversions $X_{A,k,l}$. Subsequently, the 3 ($K \times L$) linear energy balance equations (17), (21), and (28) were solved for $\theta_{F,k,l}$, $\theta_{OX,k,l}$, and $\theta_{S,k,l}$ using a Gauss elimination subroutine with pivoting. Then the electron balance equations (40) were solved to obtain new values for $\xi_{k,l}$ and the iterative procedure was repeated until all $\xi_{k,l}$ matched their previous value within 10^{-5}. This usually required 5 to 15 iterations. Most of the computations were performed with $K = L = 5$. However, the effect of unit cell clustering was explored by varying the parameter $K = L$ between 1 and 10.

Results and Discussion

The system's parameters can be divided into three groups: feed conditions (N_A, N_{O_2}, N_D, N_{N_2}, n, $T_{F,in}$, $T_{OX,in}$), reactor operating conditions (P_T, R_{ex}), and reactor design parameters (λ, b_1, b_2, c_1, c_2, δ_1, δ_2, R_e, K, L, Z). Computed

Table I. Parametric Analysis

| | perturbed parameters | | | | | | | | | | | | computed performance indicators | | | | | | | | |
run	$T_{F,in}$, K	$T_{O_2,in}$, K	N_A, μmol/cm²s	N_{O_2}, μmol/cm²s	N_D, μmol/cm²s	N_{N_2}, μmol/cm²s	c_1, cm	b_1, cm	R_{el}, ohm	R_{ex}, ohm	Z	$K' \times L'$	$\bar{X}_A$	$\bar{X}_{O_2}$	$T_{s,min}$, K	$T_{s,max}$, K	E, V	$\bar{i}$, mA/cm²	power density, W/L	η	comments
1	700	700	103	103	0	0	0.33	0.33	0.1	90.6	122	10 × 10	0.0206	0.0103	705	799	0.370	41.6	19.4	0.259	
2	600	600	500	1365	6000	5135	0.1	4.0	5 × 10⁻⁴	1.0	200	5 × 5	0.006	0.0011	600.5	603.5	0.007	3.1	0.09	0.005	effect of inlet temperature
3	720	720	500	1365	6000	5135	0.1	4.0	5 × 10⁻⁴	1.0	200	5 × 5	0.129	0.024	727.2	796.4	0.138	62.3	35.2	0.094	
4	760	760	500	1365	6000	5135	0.1	4.0	5 × 10⁻⁴	1.0	200	5 × 5	0.32	0.059	770.2	1013.3	0.341	154.2	216.3	0.233	
5	785	785	500	1365	6000	5135	0.1	4.0	5 × 10⁻⁴	1.0	200	5 × 5	0.43	0.079	797.0	1086.6	0.457	206.9	389	0.312	
6	740	740	345	941	4138	3541	0.1	4.0	5 × 10⁻⁴	1.5	200	5 × 5	0.36	0.066	749.0	1061.0	0.387	120.2	197	0.264	effect of flow rate
7	740	740	434	1186	5217	4466	0.1	4.0	5 × 10⁻⁴	1.5	200	5 × 5	0.22	0.041	748.9	874.0	0.294	91.4	114	0.200	
8	740	740	500	1365	6000	5135	0.1	4.0	5 × 10⁻⁴	1.5	200	5 × 5	0.17	0.031	748.2	839.3	0.267	83.2	94.4	0.182	
9	765	765	500	1365	6000	5135	0.1	4.0	5 × 10⁻⁴	1.0	200	5 × 5	0.35	0.064	775.5	1051.0	0.372	168	257	0.253	effect of external load
10	765	765	500	1365	6000	5135	0.1	4.0	5 × 10⁻⁴	2.0	200	5 × 5	0.21	0.038	774.1	871.4	0.432	102.3	190	0.294	
11	765	765	500	1365	6000	5135	0.1	4.0	5 × 10⁻⁴	3.0	200	5 × 5	0.17	0.031	772.6	837.9	0.501	80.4	176	0.342	
12	765	765	500	1365	6000	5135	0.1	4.0	5 × 10⁻⁴	4.0	200	5 × 5	0.14	0.026	771.6	821.0	0.560	67.9	167	0.381	
13	765	765	500	1365	6000	5135	0.1	20.0	5 × 10⁻⁴	1.0	200	1 × 1	0.50	0.091	894.8	894.0	0.528	237.6	518	0.360	effect of unit cell clustering
14	765	765	500	1365	6000	5135	0.1	5.0	5 × 10⁻⁴	1.0	200	4 × 4	0.37	0.068	777.5	1044.1	0.391	176.5	284	0.266	
15	765	765	500	1365	6000	5135	0.1	2.5	5 × 10⁻⁴	1.0	200	8 × 8	0.326	0.060	772.2	1050.7	0.347	152.5	224	0.237	
16	765	765	500	1365	6000	5135	0.1	2.0	5 × 10⁻⁴	1.0	200	10 × 10	0.322	0.059	771.1	1052.7	0.342	155.2	217	0.233	

Table II. Parameters Which Were Left Unperturbed during the Computations

$n = 2$ (for CO oxidation)
$\delta_1 = \delta_2 = 10^{-2}$ cm
$b_1 = b_2$
$c_1 = c_2 = 10^{-3}$ m (except for run 1)
$\lambda = 1$ (series connection)
$T_{ox,in}/T_{F,in} = 1$

Table III. Numerical Values of System Properties Used during the Computations

$\Delta H^\circ = -283\,130$ J/mol of A
$\Delta S^\circ = -86.83$ J/K mol of A
$C_{p,A} = C_{p,B} = C_{p,O_2} = C_{p,N_2} = C_{p,D} = 32$ J/K mol
$k_s = 2.09$ J/s m K
$h_F = h_{OX} = 0.253[(b_1 + c_1)/2b_1c_1]$ J/m² s K (b_1, c_1, in m)
$\rho = 4.17 \times 10^{-5} \exp(9700/T)$ ohm m

performance indicators included $\bar{X}_A$, $\bar{X}_{O_2}$, $T_{s,k,l}$, E, $i_{k,l}$, $\bar{i}$, η, and the power density of the assembly.

No formal optimization of the parameters was attempted. Instead, individual feed, operating, and design parameters were perturbed to assess their influence on the computed performance parameters.

The parameters which were left unperturbed are listed in Table II, while the numerical values of various physical, chemical, and thermodynamic properties, which entered the calculations, are shown in Table III.

The general behavior of the system is illustrated in Figure 3 (solid temperature distribution) and Figure 4 (current density distribution). It corresponds to a typical run, i.e., run 1 of Table I.

Both the solid temperature and the current density surfaces are nearly symmetrical about the xy angle bisector, because equal fuel and (undiluted) oxygen flow rates were used. It can be seen that significant temperature gradients can develop within the monolith, accompanied by significant gradients in current density.

Unless fuel or oxygen starvation occurs inside the monolith, the minimum and maximum solid temperatures as well as current densities occur in the (1,1) and (K,L) unit cells, respectively.

Effect of Inlet Temperature. Runs 2 to 5 (with 7.7 vol % CO in N_2) were carried out to study the effects of inlet fuel and oxidant (air) temperatures. For the conditions of these runs, the effect of inlet temperature on the solid temperatures (maximum and minimum) is shown in Figure 5. As the feed temperature increases the nonisothermality of the reactor is accentuated, together with increasing temperature gradients in the structure.

As shown in Figure 5, the difference in gaseous and solid temperatures is small, typically 1–3 K, and becomes significant only at high inlet temperatures.

With increasing feed temperatures, Table I and Figure 5 indicate that the feed and oxygen conversion, mean current density, voltage, and power density increase dramatically. This is due to the exponential dependence of electrolyte resistivity on temperature, which by far outweighs the corresponding decrease in E_{rev} (due to the negative ΔS) of this reaction system.

Effect of Gas Flow Rate. Figure 6 and runs 6 to 8 of Table I show the effect of increasing the flow rates of the fuel and oxidant streams on the temperature distribution in the monolith structure. As expected, increased space velocities make the reactor more isothermal by decreasing the maximum solid temperature. This results in decreased conversion, current density, voltage, power density, and thermodynamic efficiency.

Effect of External Resistance. Figure 7 shows that the external resistance has a pronounced effect on mono-
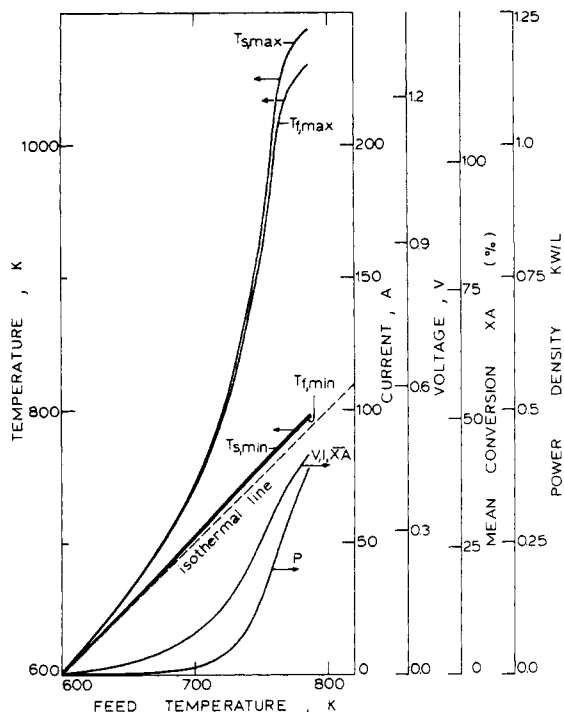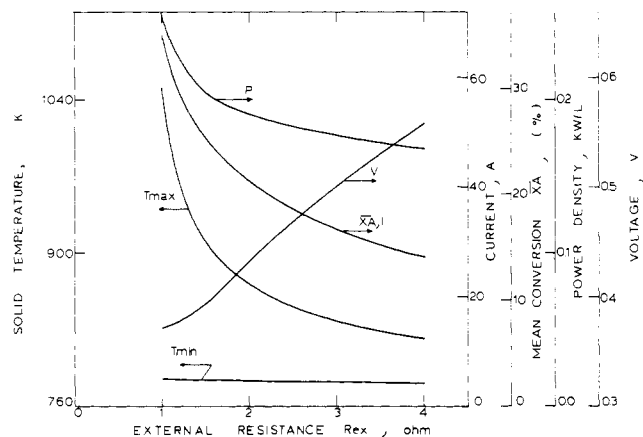
Figure 5. Effect of inlet fuel temperature on the maximum and minimum solid and fuel temperature and on current, unit cell voltage, mean fuel conversion, and power density of a (20.1 × 20.1 × 44 cm) cross-flow monolith; conditions shown in runs 2–6 of Table I.
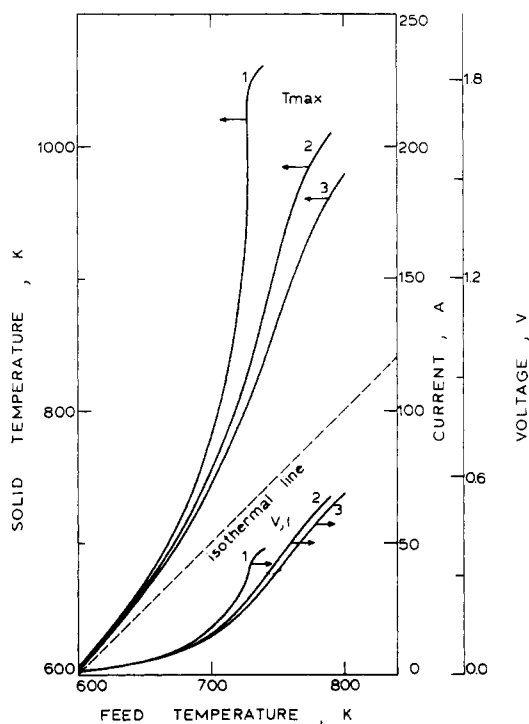

Figure 6. Effect of flow rate and inlet fuel temperature on maximum solid temperature, current, and unit cell voltage of a (20.1 × 20.1 × 44 cm) cross-flow monolith. Curves 1, 2, 3 correspond to the flow rates of runs 6, 7, 8, respectively, of Table I; other conditions shown in runs 6–8 of Table I.

lith temperature and on fuel conversion. For the conditions of these runs (runs 9–12 in Table I), the adiabatic temperature rise for complete conversion in a chemical reactor would be around 350 K. The external resistance R_{ex} "freezes" the reactor, both by reducing the rate of the reaction and by allowing only a fraction $(1 - \eta)$ of the reaction enthalpy change $(-\Delta H^{\circ})$ to be converted into heat.

Figure 7. Effect of external resistance on the maximum and minimum solid temperature, current, mean fuel conversion, unit cell voltage, and power density of a (20.1 × 20.1 × 44 cm) cross-flow monolith; see runs 9–12 of Table I for conditions.
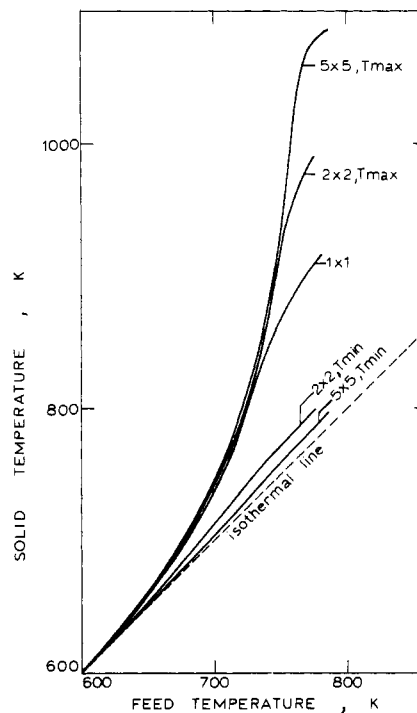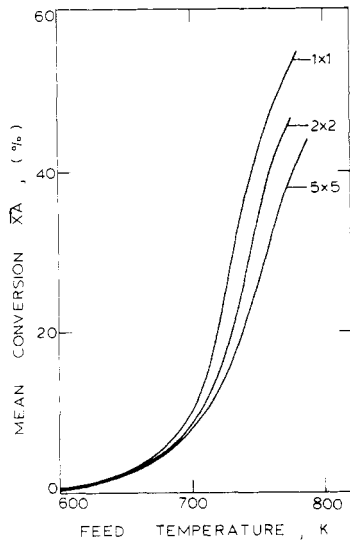

Figure 8. Effect of inlet fuel temperature on the maximum and minimum solid temperature of a (20.1 × 20.1 × 44 cm) cross-flow monolith modeled as a (1 × 1), (2 × 2), and (5 × 5) two-dimensional array of computational cells; see runs 13–16 of Table I for conditions.

Under the conditions of runs 9–12, increasing external resistance causes an increase in the operating cell voltage, despite the decrease in monolith current. This is because reactor voltage is the product of external resistance times reactor current (eq 41) and the increase in the former outweights the decrease in the latter. However, the electrical power produced decreases with increasing external resistance (as discussed before, this is not a general conclusion).

Effect of Unit Cell Clustering. The computational time required for the numerical solution of the 6 $(K \times L)$ + 1 coupled algebraic equations of a $K \times L \times Z$ geometric unit cell structure is dominated almost entirely by the time required to solve the 3 $(K \times L)$ linear energy balances during each iteration. This poses a serious problem if the cross-flow reactor consists of a large number of geometric unit cells (e.g., $K = L = 100$) since, even with $K = L = 10$, each run requires considerable computational time and since the computational time increases as $(K \times L)^2$.

**Figure 9.** Effect of inlet temperature on the mean fuel conversion in a (20.1 × 20.1 × 44 cm) cross-flow monolith modeled as a (1 × 1), (2 × 2), and (5 × 5) two-dimensional array of computational cells; see runs 13–16 of Table I for conditions.
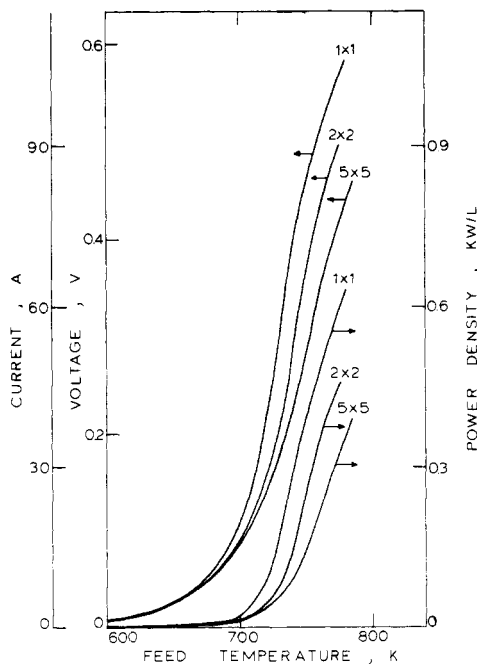
Figure 10. Effect of inlet fuel temperature on the current, unit cell voltage, and power density of a (20.1 × 20.1 × 44 cm) cross-flow monolith modeled as a (1 × 1), (2 × 2), and (5 × 5) two-dimensional array of computational cells; see runs 13–16 of Table I for conditions.

It was therefore decided to examine the effect of geometric unit cell clustering into larger computational unit cells, in order to explore the possibility of treating a $K \times L$ (e.g., 100 × 100) geometric unit cell monolith as a $K' \times L'$ (e.g., 5 × 5) computational unit cell assembly.

Figure 8 shows the effect of inlet temperature on the maximum and minimum cell temperature of a 20.1 × 20.1 × 44 cm cross-flow monolith modeled as a (1 × 1), (2 × 2), and (5 × 5) array of computational unit cells. Feed conditions are the same with those of runs 13 through 16, Table I. The corresponding effect on mean fuel conversion is shown in Figure 9, while the effects on monolith current, voltage, and power density are shown in Figure 10. It can be seen that decreasing the number of computational cells from 25 to 4 to 1 causes a substantial increase in the predicted fuel conversion, current, voltage, and power density. This is because a decrease in the number of
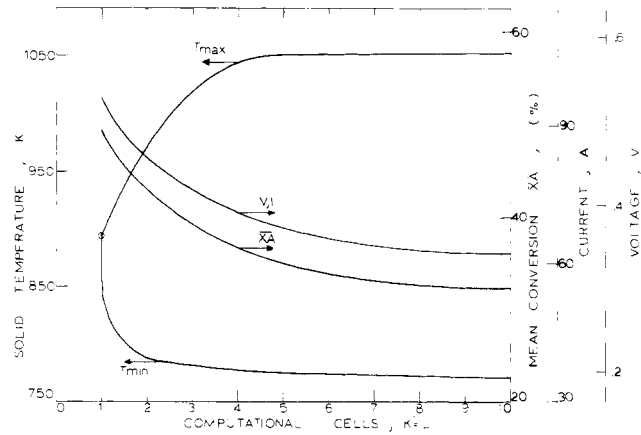
Figure 11. Effect of increasing the number of computational cells $(K' \times L')$ in a (20.1 × 20.1 × 44 cm) cross-flow monolith structure; see runs 13–16 of Table I for conditions.

computational cells enhances the effective heat backmixing in the structure, since temperature is assumed uniform within each computational cell.

However, as shown in Figure 11, the predicted fuel conversion and monolith current, voltage, and power density become insensitive to the number of computational cells once $K' = L'$ exceeds approximately 6. This result is of great practical importance, as it shows that unit cell clustering into larger computational cells can be used successfully to describe the behavior of the cross-flow monolithic electrochemical reactor and to significantly reduce computational time, provided the number of computational cells $K' \times L'$ is not decreased below approximately 6 × 6. This conclusion was reached by examining not only the results of Figure 11, which correspond to a single steady state, but also similar results of several other steady states obtained with various values of the design and operating parameters. It should be noticed that the slight residual decrease in the computed reactor performance indicators with increasing $K' = L'$ above $K' = L' = 5$ can be attributed almost entirely to the corresponding small decrease in active electrolyte area, since all the runs correspond to invariant reactor size; therefore, increasing number of computational cells corresponds to increasing number of vertical channel walls, thus slightly decreasing the active electrolyte surface area.

Summary

A mixing cell approach was used to model cross-flow monolithic solid-state electrochemical reactors. The resulting set of algebraic equations was solved numerically for the case of anodic CO oxidation in stabilized zirconia electrolyte cells. Table I, which summarizes some of the results, shows combinations of feed, operating, and design parameters which provide power densities of order 0.5 kW/L at high thermodynamic efficiencies (around 30%). Power densities exceeding 2 kW/L have also been computed for smaller size monolithic structures operating at temperatures near 1200 K. The high power densities underscore the advantage of the high surface-to-volume ratio of the cross-flow monolith geometry.

A small seven-plate (3 × 3 × 1.09 cm) experimental reactor has been constructed and tested with 5% H_2 in He as fuel and air as oxidant (Hegedus et al., 1983). The plates were electrically connected in series, with three and four plates in parallel, respectively. The operating range was 981–1113 K, and the measured current–voltage curves exhibited predominantly ohmic behavior. While the results were in general agreement with the trends predicted by the model, a direct comparison with the model was not

attempted because several of the parameters were not measured or controlled.

Nomenclature

A = fuel
B = oxidation product
b_1 = unit cell dimension; see Figure 2
b_2 = unit cell dimension; see Figure 2
c_1 = unit cell dimension; see Figure 2
c_2 = unit cell dimension; see Figure 2
C_P = specific heat, J/mol K
D = diluent in fuel stream
E = unit cell operating voltage, V
E_{rev} = reversible Nernst voltage, V
$E°$ = reversible Nernst voltage at unit activity of reactants and products, V
E_{th} = thermoneutral voltage, V
$E_{act.}$ = activation energy for O^{2-} conduction in solid electrolyte, J/mol K
F = Faraday constant, 96 484 C/mol
h = gas–solid heat transfer coefficient, J/m^2 s K
I = current, A
$\bar{i}$ = mean current density, A/m^2
$i_{k,l}$ = current density of (k,l) element, A/m^2
k = solid thermal conductivity, J/s m K
K = number of unit cells in x direction
L = number of unit cells in y direction
$N_{j,j=1 \ ... \ 18}$ = dimensionless numbers defined in text
N_A = feed fuel molar flux, mol/m^2 s
N_D = fuel diluent molar flux, mol/m^2 s
N_{O_2} = feed oxygen molar flux, mol/m^2 s
N_{N_2} = nitrogen molar flux, mol/m^2 s
n = stoichiometric coefficient in eq 1
P = power output, W
$P°_{O_2}$ = feed oxygen partial pressure, bar
P_T = operating pressure, bar
R = gas constant, 8.3105 J/mol K
$R_{k,l}$ = resistance of (k,l) element, ohm
R_e = resistance of electrical connection between unit batteries, ohm
R_{ex} = external resistive load, ohm
S = oxygen ion transfer area per unit reactor volume, cm^2/cm^3
T = temperature, K
$T_{F,in}$ = fuel feed temperature, K
$T_{OX,in}$ = oxidant feed temperature, K
T_F, T_{OX}, T_S = fuel, oxidant, and solid temperatures, K
W = electrical work produced per mole of A, J
X_A = fuel conversion

$\bar{X}_A$ = mean exit fuel conversion
X_{O_2} = oxygen conversion
$\bar{X}_{O_2}$ = mean exit oxygen conversion
Z = number of unit batteries in z direction

Greek Symbols

δ_1 = horizontal electrolyte wall thickness, m
δ_2 = vertical electrolyte wall thickness, m
ΔG = Gibbs energy change of reaction 1, J/mol of A
$\Delta H°$ = standard enthalpy change of reaction 1, J/mol of A
$\Delta S°$ = standard entropy change of reaction 1, J/mol of A K
η = cell efficiency, E/E_{TH}
θ = dimensionless temperature, $T/T_{F,in}$
λ = 1 for series connection and = 2 for parallel connection of unit batteries
$\xi_{k,l}$ = dimensionless current density
ρ = electrolyte resistivity, ohm m
ρ_0 = electrolyte resistivity at $T_{F,in}$, ohm m
$\phi_{act.}$ = activation overpotential, V
ϕ_{conc} = concentration overpotential, V
ϕ_{ohm} = ohmic overpotential, V

Subscripts

F = fuel stream
OX = oxidant stream
S = solid
in = inlet conditions

Superscript

° = standard conditions

Literature Cited

Archer, D. H.; Alles, J. J.; English, W. A.; Elikan, L.; Sverdrup, E. F.; Zahradnik, R. L. *Adv. Chem. Ser.* **1965**, *47*, 332.
Debenedetti, P. G. M.S. Thesis, Massachusetts Institute of Technology, Cambridge, MA 1981.
Debenedetti, P. G.; Vayenas, C. G. *Chem. Eng. Sci.* **1983**, *38*(11), 1817.
Degnan, T. F.; Wei, J. *AIChE J.* **1979**, *25*(2), 338.
Degnan, T. F.; Wei, J. *AIChE J.* **1980**, *26*(1), 60.
Etsell, T. H.; Flengas, S. N. *J. Electrochem. Soc.* **1971**, *118*(12), 1980.
Farr, R. D.; Vayenas, C. G. *J. Electrochem. Soc.* **1980**, *127*(7), 1478.
Federmann, E. F.; Isenberg, A. O.; Summers, W. A.; Vidt, E. J.; Feduska, W. DOE/ET/11305-T8 Feb 25, 1981.
Gur, T. M.; Huggins, R. A. *J. Electrochem. Soc.* **1979**, *126*(6), 1067.
Gur, T. M.; Huggins, R. A. *Solid State Ionics* **1981**, *5*, 563.
Hegedus, L. L.; Vayenas, C. G.; Michaels, J. unpublished results, 1983.
Lee, S. T.; Aris, R. *Chem. Eng. Sci.* **1977**, *32*, 822.
Roy, D.; Gidaspow, D. *Chem. Eng. Sci.* **1972**, *27*, 779.
Roy, D.; Gidaspow, D. *Chem. Eng. Sci.* **1974**, *29*, 2101.
Sigal, C. T.; Vayenas, C. G. *Solid State Ionics* **1981**, *5*, 567.
Stoukides, M.; Vayenas, C. G. *ACS Symp. Ser.* **1982**, *178*, 181.
Vayenas, C. G.; Farr, R. D. *Science* **1980**, *208*, 593.
Weissbart, J.; Smart, W. H.; Wydeven, T. *Aerosp. Med.* **1969**, *40*, 136.
Yang, Y.; Debenedetti, P. G.; Britt, H.; Vayenas, C. G.; Evans, L. B. Proceedings, International Symposium on Process Systems, Soc. Chem. Eng. (Japan), Tokyo, 1982.